

Hybrid quantum-gap-estimation algorithm using a filtered time series

Woo-Ram Lee ^{1,*}, Ryan Scott,² and V. W. Scarola ²

¹*Murray Associates of Utica, Utica, New York 13501, USA*

²*Department of Physics, Virginia Tech, Blacksburg, Virginia 24061, USA*



(Received 6 February 2023; accepted 15 April 2024; published 1 May 2024)

Quantum simulation advantage over classical memory limitations would allow compact quantum circuits to yield insight into intractable quantum many-body problems, but the interrelated obstacles of large circuit depth in quantum time evolution and noise seem to rule out unbiased quantum simulation in the near term. We prove that classical postprocessing, i.e., long-time filtering of an offline time series, exponentially improves the circuit depth needed for quantum time evolution. We apply the filtering method to the construction of a hybrid quantum-classical algorithm to estimate energy gap, an important observable not governed by the variational theorem. We demonstrate, within an operating range of filtering, the success of the algorithm in a proof-of-concept simulation for finite-size scaling of a minimal spin model. Our findings set the stage for unbiased quantum simulation to offer memory advantage in the near term.

DOI: [10.1103/PhysRevA.109.052403](https://doi.org/10.1103/PhysRevA.109.052403)

I. INTRODUCTION

Quantum simulation not only offers the potential to speed up solutions to otherwise intractable quantum many-body problems but can also yield significant memory advantages in comparison to classical algorithms [1–3]. Unbiased (exact) classical methods, such as exact diagonalization applied to a time-independent Hamiltonian matrix H , can, in principle, be used to perform finite-size extrapolation of important observables to benchmark approximations, compare with experiment, or map out phase diagrams. On the other hand, the exponential increase in Hilbert-space size of quantum many-body problems severely limits accessible system sizes (i.e., particle or orbital numbers) on classical machines due to memory constraints. The same exponential Hilbert-space increase can be leveraged as a memory advantage [4] by unbiased quantum simulation to compete with classical algorithms on appropriately chosen models [5]. The considerable memory advantage of quantum devices suggests that finite-size quantum simulation could, even in the near term, outperform classical machines in unbiased calculations.

The quantum-phase-estimation (QPE) [2,3,6] family of algorithms yields unbiased estimates of various quantities, including energy eigenvalues [7–14] and energy gaps [15–19]. QPE conventionally relies on the Trotter-Suzuki decomposition [20,21] to implement the time propagator e^{-iHt} with quantum circuits. Unfortunately, the circuit depth needed to implement time evolution is known to scale rather prohibitively for a speedup advantage [22–26], thus casting doubt on prospects for compact circuit design with QPE. Furthermore, uncorrected noise in large-depth QPE-based circuits will erode coherence.

The interrelated obstacles of large circuit depth and noise led to efforts to develop alternative approaches to QPE. Variational quantum eigensolvers (VQEs) [24,27,28] turned out to yield noise-tolerant, but biased, estimates of ground-state energy levels. A VQE requires only shallow quantum circuits but has sustaining issues, e.g., the Barren plateaus that plague the cost-function landscape in scale up [29]. Another approach starts from the assumption of large numbers of fault-tolerant qubits while designing improvements to the scaling of circuit depth. Such “top-down” approaches have made considerable progress (see Ref. [30] for a review) but, nonetheless, rely on assumptions of high qubit overhead to implement active error correction even on just one single-qubit noise channel [31]. On the other hand, QPE can be revisited from the perspective of hybrid quantum-classical circuits designed for scaling up small noisy quantum devices (“bottom-up approach”) for memory advantage (as opposed to speedup advantage). In this approach, as in the case of VQEs, classical postprocessing is essential, but has more focus on unbiased estimates of solutions [11–14].

In this work, we propose a hybrid quantum-gap-estimation (QGE) algorithm using a filtered time series, built from quantum circuits and postprocessed using the classical Fourier transform to return energy gaps. The hybrid QGE algorithm has useful features. First, the quantum circuit remains compact by avoiding calls to ancilla qubits, quantum Fourier transforms, and quantum state tomography. Second, the solution provides an unbiased estimate of energy gaps beyond the rigorous applicability of the variational theorem. Last, the filter in postprocessing is used to maximize simulation performance within the operating range.

Time-series filters, allowing nonunitary evolution of quantum systems, have been implemented in different contexts such as ground-state energy estimation using the approximate cumulative distribution function [11,12] and hybrid dynamical mean-field theory (DMFT) with an impurity solver

*wrlee@murrayau.com

processed online [32–34]. To our knowledge, however, the role of the filter in gap estimation has not been explored yet. In this work, we show that the filter *exponentially* improves circuit depth at long times. We demonstrate the performance boost of the hybrid QGE algorithm with time-series filters in proof-of-concept simulations. The noise resilience of the algorithm will be discussed in a separate work [35].

This paper is outlined as follows. In Sec. II, we derive the formula for Trotter truncation error in association with a time-series filter and reveal the impact on the upper bound of (Trotter) circuit depth. In Sec. III, we describe the hybrid QGE algorithm. In Sec. IV, we demonstrate the simulation results for the gap of a minimal spin model and the gap-based phase diagram using finite-size extrapolation. We conclude in Sec. V.

II. FILTERED QUANTUM TIME EVOLUTION

A. Trotter truncation error with filtering

QPE-based algorithms leverage the enlarged Hilbert space on quantum devices for evaluation of the time propagator. But intractable Hamiltonians with noncommuting terms, e.g., $H = H_1 + H_2$, where $[H_1, H_2] \neq 0$, are nontrivial to time evolve. Exact time evolution is described by the time propagator $U_{\text{exact}}(t) = e^{-iHt}$. Hereafter, we set $\hbar = 1$. The Trotter-Suzuki formula offers various levels of approximation, set by the order p , to $U_{\text{exact}}(t)$ [20,21]:

$$U_M^{(p)}(t) = [U^{(p)}(t_M)]^M, \quad (1)$$

where $t_M = t/M$, $M \in \mathbb{N}$, and a single sequence of unitaries is defined by

$$U^{(1)}(t) = e^{-iH_1 t} e^{-iH_2 t}, \quad (2)$$

$$U^{(2)}(t) = e^{-iH_1 t/2} e^{-iH_2 t} e^{-iH_1 t/2}, \quad (3)$$

$$U^{(2q)}(t) = [U^{(2q-2)}(\kappa_{2q} t)]^2 U^{(2q-2)}[(1 - 4\kappa_{2q})t] \times [U^{(2q-2)}(\kappa_{2q} t)]^2, \quad (4)$$

with $\kappa_{2q} = (4 - 4^{1/(2q-1)})^{-1}$ for $q \geq 2$. Equations (1)–(4) yield precise results once the Trotter depth M exceeds a certain cutoff M_c . The $p = 1$ formula is especially fit to run on resource-limited noisy quantum devices. Progress in estimating Trotter truncation error [22,23,36–38] allows us to prove significant improvements in the required cutoff of M .

In this section, we prove that long-time filtering of the time propagator leads to substantial improvement in Trotter depth. To start, we take $H \rightarrow H + \Sigma(t)$, where $\Sigma(t)$ defines the self-energy describing energy relaxation to the environment. Here, we choose a minimal model [39,40]: $\Sigma(t) = -i\Gamma(t)I/2$, where $\Gamma(t) > 0$ is a user-defined control function to select specific time bins and I is the identity matrix.

We apply the method in Ref. [23] to derive, in the presence of filtering, the leading correction to $U_{\text{exact}}(t)$ by Trotter truncation error and thereby the upper bound of M . We consider the first-order inhomogeneous differential equation for $\mathcal{U}(t)$:

$$\frac{d}{dt}\mathcal{U}(t) + i\mathcal{H}(t)\mathcal{U}(t) = \mathcal{R}(t), \quad (5)$$

where $\mathcal{H}(t)$ and $\mathcal{R}(t)$ are continuous operator-valued functions of $t \in \mathbb{R}$. The solution, using variation of parameters, reads

$$\mathcal{U}(t) = T e^{-i \int_0^t d\tau \mathcal{H}(\tau)} \mathcal{U}(0) + \int_0^t d\tau_1 T e^{-i \int_{\tau_1}^t d\tau_2 \mathcal{H}(\tau_2)} \mathcal{R}(\tau_1), \quad (6)$$

where T is the time-ordering operator. To proceed further with $\mathcal{R}(t)$, we can refer back to Eq. (5). For the application to our problem, we take $\mathcal{U}(t) \rightarrow e^{-\int_0^t d\tau \Gamma(\tau)/2} U_M^{(p)}(t)$ and $\mathcal{H}(t) \rightarrow H - i\Gamma(t)I/2$ and factor out the term $e^{-\int_0^t d\tau \Gamma(\tau)/2}$ from both sides of Eq. (6). The equation for $U_M^{(p)}(t)$ is then arranged into the form

$$U_M^{(p)}(t) = U_{\text{exact}}(t) + \delta U_M^{(p)}(t), \quad (7)$$

where the correction term is given by

$$\delta U_M^{(p)}(t) = \int_0^t d\tau U_{\text{exact}}(t - \tau) [\Xi_M^{(p)}(\tau) + \Theta_M^{(p)}(\tau)], \quad (8)$$

with two functions defined in the expansion form:

$$\Xi_M^{(p)}(t) = \frac{1}{M} \sum_{l=0}^{M-1} [U^{(p)}(t_M)]^l \left\{ \left(\frac{d}{dt_M} + iH \right) U^{(p)}(t_M) \right\} \times [U^{(p)}(t_M)]^{M-l-1}, \quad (9)$$

$$\Theta_M^{(p)}(t) = \left\{ iH - \frac{1}{M} \sum_{l=0}^{M-1} [U^{(p)}(t_M)]^l iH [U^{(p)}(t_M)]^{-l} \right\} \times [U^{(p)}(t_M)]^M. \quad (10)$$

Equation (9) gives the leading correction to $U_{\text{exact}}(t)$. To proceed, it is convenient to define the adjoint derivative, $\text{ad}_A B = [A, B]$, along with the related identities $e^{x \text{ad}_A} B = e^{xA} B e^{-xA}$ and $\frac{d^n}{dx^n} e^{x \text{ad}_A} B = e^{x \text{ad}_A} \text{ad}_A^n B$, where A and B are matrices and x is a scalar. For $p = 1$, we find

$$\left(\frac{d}{dt_M} + iH \right) U^{(1)}(t_M) = e^{-iH_1 t_M} V^{(1)}(t_M) e^{-iH_2 t_M}, \quad (11)$$

where we define

$$V^{(1)}(t_M) = (e^{t_M \text{ad}_{iH_1}} - 1) iH_2. \quad (12)$$

Since Eq. (12) satisfies the order condition $O(t_M)$, it can be represented in the integral form of the Taylor remainder:

$$V^{(1)}(t_M) = \int_0^{t_M} d\tau e^{\tau \text{ad}_{iH_1}} \text{ad}_{iH_1} iH_2. \quad (13)$$

Similarly, the result for $p = 2$ reads

$$\left(\frac{d}{dt_M} + iH \right) U^{(2)}(t_M) = e^{-iH_1 t_M/2} V^{(2)}(t_M) \times e^{-iH_2 t_M} e^{-iH_1 t_M/2}, \quad (14)$$

where we define

$$V^{(2)}(t_M) = -(e^{t_M \text{ad}_{-iH_2}} - 1) iH_1/2 + (e^{t_M \text{ad}_{iH_1/2}} - 1) iH_2. \quad (15)$$

Under the order condition $O(t_M^2)$, Eq. (15) is recast as

$$V^{(2)}(t_M) = \int_0^{t_M} d\tau \int_0^\tau d\tau' \left(-e^{\tau' \text{ad}_{-iH_2}} \text{ad}_{-iH_2}^2 iH_1/2 + e^{\tau' \text{ad}_{iH_1/2}} \text{ad}_{iH_1/2}^2 iH_2 \right). \quad (16)$$

For $p \geq 4$, however, complexity increases. At $p = 4$, Eq. (4), for example, has a sequence of 11 unitaries. Here, for our purpose, we just refer to the result in Ref. [23]. Last, we note that Eq. (10) can be safely ignored because it gives the subleading correction to $U_{\text{exact}}(t)$.

In the context of quantum simulation, we consider the trace distance between the exact and Trotterized output states on quantum circuits. In our setup, the output states are represented in the density-matrix form:

$$\rho_{\text{exact}}(t) = U_1^\dagger U_{\text{exact}}(t) U_1 \rho_0 U_1^\dagger U_{\text{exact}}^\dagger(t) U_1, \quad (17)$$

$$\rho_M^{(p)}(t) = U_1^\dagger U_M^{(p)}(t) U_1 \rho_0 U_1^\dagger [U_M^{(p)}(t)]^\dagger U_1, \quad (18)$$

where U_1 acts on input registers ρ_0 for initial-state preparation. We plug Eq. (7) in Eq. (18) to find the expansion:

$$\rho_M^{(p)}(t) = \rho_{\text{exact}}(t) + \delta\rho_M^{(p)}(t) + O[(\delta\rho_M^{(p)})^2], \quad (19)$$

where the correction term is given by

$$\delta\rho_M^{(p)}(t) = U_1^\dagger \delta U_M^{(p)}(t) U_1 \rho_0 U_1^\dagger [U_{\text{exact}}(t)]^\dagger U_1 + U_1^\dagger U_{\text{exact}}(t) U_1 \rho_0 U_1^\dagger [\delta U_M^{(p)}(t)]^\dagger U_1. \quad (20)$$

In the presence of filtering, we take $\rho(t) \rightarrow \mathcal{F}(t)\rho(t)$ and set Trotter truncation error to $\varepsilon_T^{(p)} \equiv \|\mathcal{F}(t)[\rho_M^{(p)}(t) - \rho_{\text{exact}}(t)]\|$, where $\|A\|$ is the spectral norm, i.e., the largest singular value of matrix A . $\mathcal{F}(t)$ defines the filter:

$$\mathcal{F}(t) = e^{-\int_0^t d\tau \Gamma(\tau)}, \quad (21)$$

which is exemplified by the Lorentzian filter, $\mathcal{F}_L(t) = e^{-\eta t}$ for $\Gamma(t) = \eta$, and the Gaussian filter, $\mathcal{F}_G(t) = e^{-\sigma^2 t^2/2}$ for $\Gamma(t) = \sigma^2 t$, where $\eta = \sigma\sqrt{2\ln 2}$. To estimate the bound of $\varepsilon_T^{(p)}$, we use the properties of the spectral norm: $\|cA\| = |c|\|A\|$, $\|AB\| \leq \|A\|\|B\|$, $\|A+B\| \leq \|A\| + \|B\|$, and $\|e^{iA}\| = 1$ if $A = A^\dagger$, where A and B are matrices and c is a scalar. The multiple integrals are then simplified. For example, $\int_0^t d\tau \int_0^\tau d\tau' = t^2/(2M)$ for $p = 1$, and $\int_0^t d\tau \int_0^\tau d\tau' \int_0^\tau d\tau'' = t^3/(6M^2)$ for $p = 2$. The result is summarized by

$$\varepsilon_T^{(p)} \leq C^{(p)} \frac{t^{p+1} \mathcal{F}(t)}{M^p}, \quad (22)$$

where the prefactors are defined by

$$C^{(1)} = \|[H_1, H_2]\|, \quad (23)$$

$$C^{(2)} = \sum_{\gamma \in \{1,2\}} c_\gamma^{(2)} \|[H_\gamma, [H_1, H_2]]\|, \quad (24)$$

$$C^{(4)} = \sum_{\gamma, \lambda, \mu \in \{1,2\}} c_{\gamma\lambda, \mu}^{(4)} \|[H_\gamma, [H_\lambda, [H_\mu, [H_1, H_2]]]]\|, \quad (25)$$

with numerical constants $c_1^{(2)} = 0.083$, $c_2^{(2)} = 0.167$, $c_{111}^{(4)} = 0.0094$, $c_{112}^{(4)} = 0.0114$, $c_{121}^{(4)} = 0.0092$, $c_{122}^{(4)} = 0.0148$, $c_{211}^{(4)} = c_{212}^{(4)} = 0.0194$, $c_{221}^{(4)} = 0.0346$, and $c_{222}^{(4)} = 0.0568$. We

note that, at small times, the upper bound in Eq. (22) scales in a different polynomial order of t for each choice of p . $\mathcal{F}(t)$ can be used to control the long-time behavior of the bound such that overall suppression is achieved. The role of $\mathcal{F}(t)$ can be addressed more clearly in Fourier space (see Sec. III C).

Finally, as a consequence of Eq. (22), we find that the total depth for Trotter circuits is bounded above by the cutoff $D_c^{(p)} = N_g^{(p)} M_c^{(p)}$, where $N_g^{(p)}$ counts unitary gates per Trotter iteration and $M_c^{(p)}$ is the Trotter depth cutoff for a fixed $\varepsilon_{T,c}^{(p)} = \varepsilon_{T,c}^{(p)}$.

$$M_c^{(p)}[\mathcal{F}(t)] = \left(\frac{C^{(p)}}{\varepsilon_{T,c}^{(p)}} \right)^{1/p} t^{1+1/p} [\mathcal{F}(t)]^{1/p}. \quad (26)$$

This is one of our central results because it allows us to choose $\mathcal{F}(t)$ to relax otherwise stringent conditions on circuit depth in QPE-based simulation.

B. Example: One-dimensional transverse-field Ising model

To estimate $M_c^{(p)}$, and therefore $D_c^{(p)}$, we consider the transverse-field Ising model (TFIM) in one dimension:

$$H_1 = -J \sum_{j=0}^{N-2} \sigma_j^z \sigma_{j+1}^z, \quad H_2 = -h \sum_{j=0}^{N-1} \sigma_j^x, \quad (27)$$

where σ^α , with $\alpha \in \{x, y, z\}$, are the Pauli matrices; N is the number of spins at sites $j \in [0, N-1]$; J is the Ising coupling; and h is the magnetic field. The TFIM has a paramagnetic ground state (for $J/h < 1$) separated from a ferromagnetic state (for $J/h > 1$) by a quantum critical point (at $J/h = 1$) [41]. Straightforward calculations using Eq. (27) yield the explicit forms of the commutators in Eqs. (23)–(25) and the bounds of the spectral norms. See Appendix A for details.

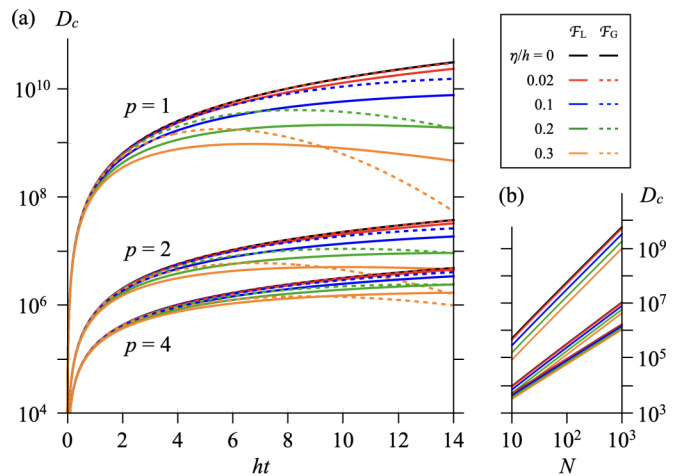


FIG. 1. (a) Plot of the upper bound of total circuit depth D_c (= Trotter depth cutoff \times gate counts per iteration) versus time for the TFIM ($N = 10^3$) with different choices for the Trotterization order $p \in \{1, 2, 4\}$ and the filter $\mathcal{F} \in \{\mathcal{F}_L, \mathcal{F}_G\}$, showing that η ($= \sigma\sqrt{2\ln 2}$) exponentially suppresses the bound over a long time. Other parameters are set to $J/h = 0.4$ and $\varepsilon_{T,c} = 10^{-2}$. The vertical axis is a log scale. (b) Plot of D_c versus N for a fixed $ht = 6$. Both axes are log scales.

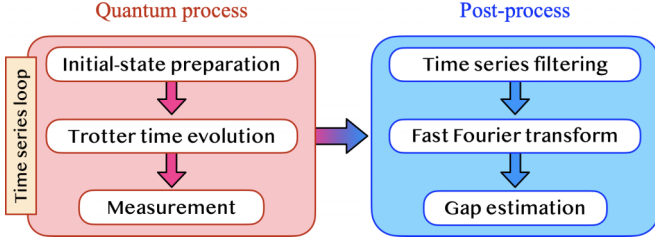


FIG. 2. Flowchart for the hybrid QGE algorithm.

Figure 1 demonstrates the impact of the filter function on the upper bound of the total circuit depth D_c for the TFIM. Here, we count $N_g^{(1)} = N$, $N_g^{(2)} = 2N - 1$, and $N_g^{(4)} = 6N - 1$ (for uncompressed circuits) and use two types of filters, \mathcal{F}_L and \mathcal{F}_G , for comparison. Without filtering ($\eta = 0$), the model shows a prohibitive Trotter scaling that appears to prevent QPE simulation on quantum devices. In Fig. 1(a), for spin counts $N = 10^3$, the top black solid curve ($p = 1$) exceeds, for example, $D_c \sim 10^7$ for $ht > 6$, which is improved to $D_c \sim 10^4 (10^3)$ for $p = 2(4)$. Figure 1(b) shows that $|D_c^{(p)} - D_c^{(p' \neq p)}|$ is reduced for smaller N . In the presence of filtering ($\eta > 0$), however, long-time evolution is truncated, and D_c is significantly improved (colored solid curves for \mathcal{F}_L and colored dashed curves for \mathcal{F}_G), thus suggesting a route to considerable improvements in QPE-based algorithms. Note that filtering is more effective for smaller p [see Eq. (26)], allowing $D_c^{(p)} > D_c^{(p')}$ for $p < p'$ in a long time. Last, D_c is only a bound. In practice, total circuit depth relies on the choice of H , \mathcal{F} , and the algorithm.

III. HYBRID QUANTUM-GAP-ESTIMATION ALGORITHM

A. Overview

We now construct a hybrid QGE algorithm and demonstrate the impact of filtering on time evolution. The algorithm flowchart is depicted in Fig. 2. We start with an input state $|\psi_1\rangle$ that overlaps with an exact state $|\psi_{\text{exact}}\rangle$ of interest, perform Trotter time evolution, and then read out in the same basis as the input state. The output state oscillates in time at frequencies of the exact energy gaps for any input state satisfying $\langle \psi_1 | \psi_{\text{exact}} \rangle \neq 0$. A classical fast Fourier transform of a time series, after being filtered, reveals exact energy gaps within the window 2η set by the filter. In the following we provide details for the quantum process and postprocess.

B. Quantum process (online)

In a quantum processor, each run is iterated over discrete time $t_n = n\delta t$, where $n \in [0, L - 1]$ for L Fourier sampling points. Figure 3 shows the quantum circuit implementation for our example, the TFIM, in a single run. The circuit proceeds in three steps. First, input qubits are prepared in quantum registers to build the initial state: $|\psi_1\rangle = U_I \prod_{j=0}^{N-1} |0\rangle_j^z$. For our purpose, the product-state unitary is a minimal choice (here, entanglement is not essential):

$$U_I(\vec{\theta}) = \prod_{j=0}^{N-1} R_j^y(\theta_j), \quad (28)$$

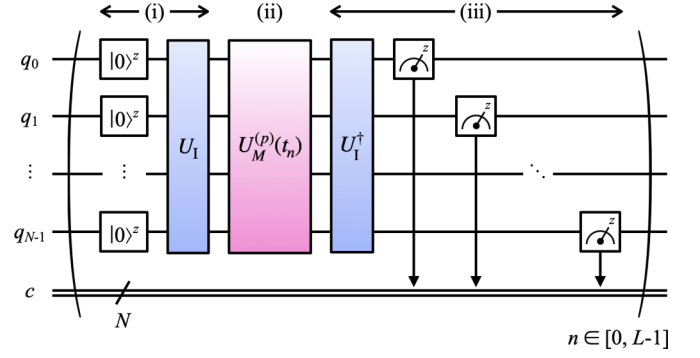


FIG. 3. Quantum circuit of the hybrid QGE algorithm for a many-body Hamiltonian H . (i) Input preparation: N qubits are prepared (and reset) in the quantum registers (q_0, q_1, \dots, q_{N-1}) and rotated by the unitary U_I to create the initial state. (ii) Trotter time evolution of the order p by the unitary $U_M^{(p)}(t_n)$. (iii) Measurement: Output qubits are rotated back to compensate U_I , and z -basis measurements are carried out to return time-series data (of size L) to the classical register, c .

where $R_j^\alpha(\theta) = \exp(-i\frac{\theta}{2}\sigma_j^\alpha)$ and $\vec{\theta} = (\theta_0, \theta_1, \dots, \theta_{N-1})$ is a free parameter that can be chosen to emphasize different gaps. Second, $|\psi_1\rangle$ is time evolved by applying a sequence of unitaries determined by H and $p \in \{1, 2, 4\}$:

$$\begin{aligned} U_M^{(1)}(t_n) &= \left[\prod_{\tilde{j}_2} R_{j_1, j_1+1}^{zz} \left(\frac{\chi_n}{M} \right) R_{j_2}^x \left(\frac{\phi_n}{M} \right) \right]^M, \\ U_M^{(2)}(t_n) &= \left[\prod_{\tilde{j}_3} R_{j_1, j_1+1}^{zz} \left(\frac{\chi_n}{2M} \right) R_{j_2}^x \left(\frac{\phi_n}{M} \right) R_{j_3, j_3+1}^{zz} \left(\frac{\chi_n}{2M} \right) \right]^M, \\ U_M^{(4)}(t_n) &= \left[\prod_{\tilde{j}_{11}} R_{j_1, j_1+1}^{zz} \left(\frac{\kappa_4 \chi_n}{2M} \right) R_{j_2}^x \left(\frac{\kappa_4 \phi_n}{M} \right) R_{j_3, j_3+1}^{zz} \left(\frac{\kappa_4 \chi_n}{M} \right) \right. \\ &\quad \times R_{j_4}^x \left(\frac{\kappa_4 \phi_n}{M} \right) R_{j_5, j_5+1}^{zz} \left(\frac{(1-3\kappa_4)\chi_n}{2M} \right) \\ &\quad \times R_{j_6}^x \left(\frac{(1-4\kappa_4)\phi_n}{M} \right) R_{j_7, j_7+1}^{zz} \left(\frac{(1-3\kappa_4)\chi_n}{2M} \right) \\ &\quad \times R_{j_8}^x \left(\frac{\kappa_4 \phi_n}{M} \right) R_{j_9, j_9+1}^{zz} \left(\frac{\kappa_4 \chi_n}{M} \right) \\ &\quad \left. \times R_{j_{10}}^x \left(\frac{\kappa_4 \phi_n}{M} \right) R_{j_{11}, j_{11}+1}^{zz} \left(\frac{\kappa_4 \chi_n}{2M} \right) \right]^M, \quad (29) \end{aligned}$$

where $\prod_{\tilde{j}_m} = \prod_{j_1} \prod_{j_2} \dots \prod_{j_m}$, $R_{j, j+1}^{zz}(\theta) = \exp(-i\frac{\theta}{2}\sigma_j^z \sigma_{j+1}^z)$, $\chi_n = -2Jt_n$, $\phi_n = -2ht_n$, and $\kappa_4 = (4 - \sqrt[3]{4})^{-1} \approx 0.414$. M repetitions are applied until Trotter error (alternatively, spectral sum or gap-estimation error; see Sec. IV A) is reduced below a tolerance. In the last online step, output qubits are rotated back to the input-state basis and measured. Here, quantum state tomography [42] or ancilla qubits [7, 17] are not involved, thus saving computational resources.

C. Postprocess (offline)

The time-evolved output state obtained from the quantum circuit is processed offline. In the first offline step, we build time-series data $\{(t_n, \mathcal{P}_n^{(p)})\}_{n=0}^{L-1}$, in which measurement outcomes in the z basis are encoded:

$$\mathcal{P}_n^{(p)} = \text{Tr}[\rho_0 \rho_{\vec{\theta}}^{(p)}(t_n)]. \quad (30)$$

Here, we define the density matrices $\rho_0 = \prod_{j=0}^{N-1} |0\rangle_j \langle 0|_j$ for the input registers and $\rho_{\vec{\theta}}^{(p)}(t_n) = U_{M, \vec{\theta}}^{(p)}(t_n) \rho_0 [U_{M, \vec{\theta}}^{(p)}(t_n)]^\dagger$ for the output with the similarity transform $U_{M, \vec{\theta}}^{(p)}(t_n) = [U_1(\vec{\theta})]^\dagger U_M^{(p)}(t_n) U_1(\vec{\theta})$. Next, Eq. (30) is filtered by $\mathcal{F}_n = \mathcal{F}(t_n)$ and fed into the classical subroutine for a discrete Fourier transform (DFT), which yields a (many-body) spectral function:

$$\mathcal{A}^{(p)}(\omega_m) = \frac{\delta t}{2\pi} \text{Re} \sum_{s=\pm} \sum_{n=0}^{L-1} e^{i\omega_m t_{sn}} \mathcal{F}_n \mathcal{P}_{sn}^{(p)}, \quad (31)$$

where we define discrete frequencies $\omega_m = m\delta\omega$, conjugate to t_n , in units of δt and $\delta\omega$, satisfying $\delta\omega\delta t = 2\pi/L$, and $m, n \in [0, L-1]$. The $s = + (-)$ terms in Eq. (31) describe causal (anticausal) processes. In practice, a fast Fourier transform is widely adopted to improve computational complexity of the original DFT, $O(N^2)$ to $O(N \log N)$ [43].

To reveal key features of Eq. (31), we consider the continuum limit ($L \rightarrow \infty$):

$$\mathcal{A}^{(p)}(\omega) = \frac{1}{2\pi} \sum_{s=\pm} \int_{-\infty}^{\infty} dt \cos(\omega t) \Theta(st) \mathcal{F}(st) \mathcal{P}^{(p)}(t), \quad (32)$$

where $\Theta(t)$ is the step function and $\mathcal{P}^{(p)}(t) = \text{Tr}[\rho_0 \rho_{\vec{\theta}}^{(p)}(t)] = |\langle \psi_1 | U_M^{(p)}(t) | \psi_1 \rangle|^2 \in \mathbb{R}$, which is distinguished from the form $\langle \psi_1 | U_M^{(p)}(t) | \psi_1 \rangle \in \mathbb{C}$ for eigenvalue estimation [44]. Equation (32) can be recast further in the convolution form,

$$\mathcal{A}^{(p)}(\omega) = \int_{-\infty}^{\infty} d\tilde{\omega} \tilde{\mathcal{F}}(\tilde{\omega}) \mathcal{A}_0^{(p)}(\omega - \tilde{\omega}), \quad (33)$$

where $\tilde{\mathcal{F}}$ represents the filter in Fourier space,

$$\tilde{\mathcal{F}}(\omega) = \frac{1}{\pi} \int_0^{\infty} dt \cos(\omega t) \mathcal{F}(t), \quad (34)$$

and $\mathcal{A}_0^{(p)}(\omega) \equiv \mathcal{A}^{(p)}(\omega)|_{\mathcal{F}=1}$ (without filtering). Two features of Eq. (33) are addressed below.

First, peak centers in $\mathcal{A}_0^{(p)}$ return exact energy gaps for all choices of H and $|\psi_1\rangle$. To show this, ignoring Trotter error for $M > M_c$, we approximate $U_M^{(p)}(t) \approx e^{-iHt}$. We then expand $|\psi_1\rangle = \sum_u c_u |u\rangle$, where eigenstates $|u\rangle$ satisfy $H|u\rangle = \mathcal{E}_u |u\rangle$ with eigenenergies \mathcal{E}_u , and plug it in $\mathcal{A}_0^{(p)}$ to derive the spectral representation (hereafter, we drop the superscript p):

$$\mathcal{A}_0(\omega) = \sum_{u,v} |c_u|^2 |c_v|^2 \delta(\omega - \Delta_{u,v}), \quad (35)$$

where we define the Dirac delta function $\delta(\omega) = \frac{1}{2\pi} \int dt e^{i\omega t}$ and exact energy gaps $\Delta_{u,v} = \mathcal{E}_u - \mathcal{E}_v$. For estimation of a target, say, $\Delta_{u,v}$, the condition of $|c_u| |c_v| \neq 0$ is generally demanded. Without loss of generality, we can drop the redundant sum over $u \leq v$ to focus on the partial sum over $u > v$.

Second, Eq. (33) converts δ functions in Eq. (35) into the line shapes set by Eq. (34):

$$\mathcal{A}(\omega) = \sum_{u,v} |c_u|^2 |c_v|^2 \tilde{\mathcal{F}}(\omega - \Delta_{u,v}). \quad (36)$$

For the choice of $\mathcal{F}_L(t) = e^{-\eta t}$, $\tilde{\mathcal{F}}(\omega)$ describes a Lorentzian line shape: $\tilde{\mathcal{F}}_L(\omega) = \frac{1}{\pi} \frac{\eta}{\omega^2 + \eta^2}$. For $\mathcal{F}_G(t) = e^{-\sigma^2 t^2/2}$, it turns out to be a Gaussian line shape: $\tilde{\mathcal{F}}_G(\omega) = \frac{1}{\sqrt{2\pi}\sigma} e^{-\frac{\omega^2}{2\sigma^2}}$. Here, the broadening 2η defines the full width at half maximum of the line shape and has a connection to σ : $\eta = \sigma\sqrt{2 \ln 2}$. It has an operating range designed to maximize simulation performance: 2η is bounded below by Trotter error ε_T and above by peak-to-peak separations to hold spectral resolutions in gap estimation. See Sec. IV B for further discussion.

The last offline step establishes a consistent gap-estimation protocol for Eq. (31). We need to start with an initial guess of the energy gap Δ_0 , e.g., mean field or perturbative. Here, we use perturbation theory for the TFIM with open boundaries: $\Delta_0/h = 2[1 - (1 - 1/N)J/h]$ (see Appendix B). (We focus on the lowest gap but can find any gap by adjusting the initial guess.) We then search for the peak center in the range $\Delta_0 - \delta\Delta/2 \leq \omega \leq \Delta_0 + \delta\Delta/2$ to find the unbiased estimate of Δ . Here, the search window $\delta\Delta$ is initially set to 2η . If Δ is not within the range, we restart with a new choice of either $\delta\Delta$ or Δ_0 . This process is iterated until a solution is found.

IV. RESULTS

So far, we have proposed a hybrid QGE algorithm using a filtered time series, thereby requiring shallow circuits. In this section, we demonstrate proof-of-concept simulation results using the TFIM with small size $N \in \{2, 3, 4, 5\}$ as a benchmark model [45]. The results are compared for different choices of the filter \mathcal{F} and Trotterization order p . Here, studying noise-induced error in quantum processes is beyond our scope. To demonstrate the algorithm, we discuss our implementation case: gaps of the TFIM and the gap-based paramagnetic phase diagram determined by finite-size extrapolation.

A. Convergence boost of QGE from filtering

The central assertion in Sec. II was that filtering Trotter time evolution at long times effectively lowers the upper bound of circuit depth for a fixed Trotter truncation error. Here, we numerically confirm that the filtering method can be leveraged to boost the convergence of the hybrid QGE algorithm.

Figure 4 shows simulation results for $N = 4$ and $J/h = 0.4$ for different choices of $p \in \{1, 4\}$ and $\mathcal{F} \in \{\mathcal{F}_L, \mathcal{F}_G\}$. Input orientations are fixed here but, later on, will be tuned for further investigation. The top panels indicate that increasing η gives better convergence of \mathcal{A} to the exact form with D . The plots with $D \ll \tilde{D}_c$, where \tilde{D}_c is the empirical bound of the circuit depth, feature satellite peaks (apart from the main peak) which are governed by the Floquet stroboscopic dynamics [47]. If the satellite peaks are separated within the resolution limit 2η , they are smoothed out, thereby leaving only the main peak behind. The black open arrow highlights

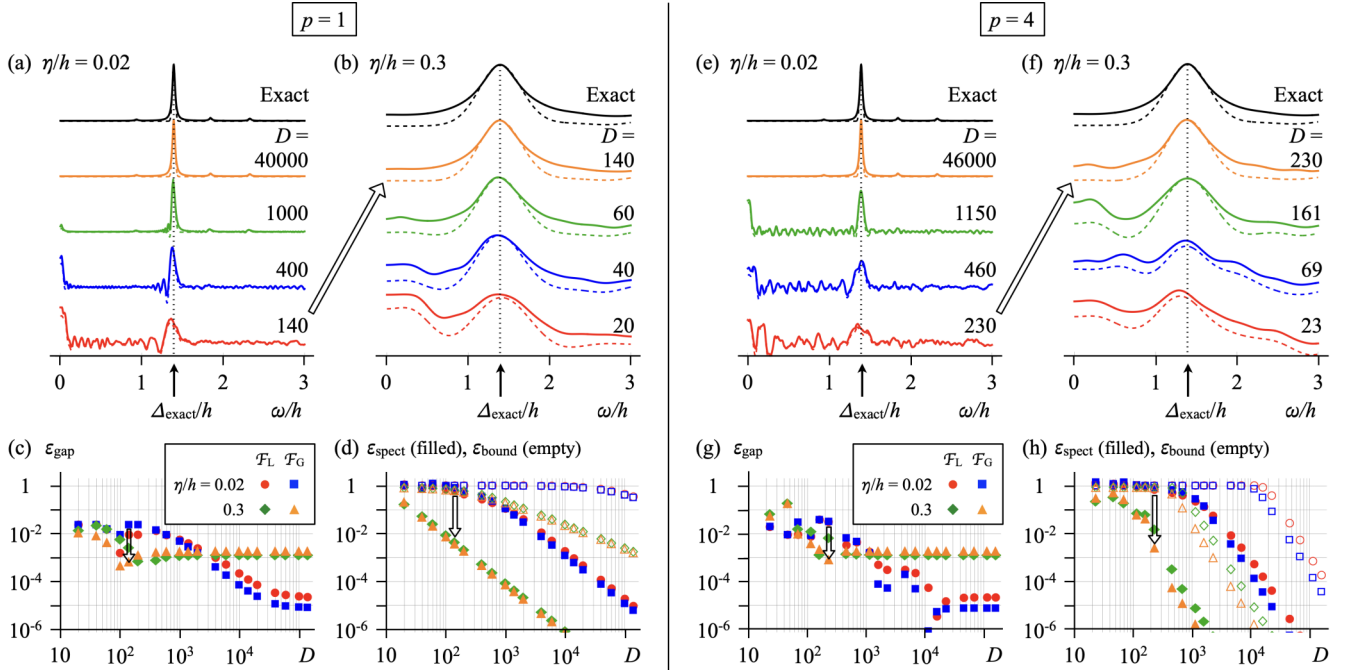


FIG. 4. Simulation results demonstrating the convergence boost of QGE by filtering. The results are compared for different choices of the Trotterization order, (a)–(d) $p = 1$ and (e)–(h) 4; the broadening, (a) and (e) $\eta/h = 0.02$ and (b) and (f) 0.3; and the filter $\mathcal{F} \in \{\mathcal{F}_L, \mathcal{F}_G\}$. The top panels show the spectral function \mathcal{A} versus frequency ω for the TFIM with $N = 4$ and $J/h = 0.4$. Colored solid (dashed) curves are the results for $\mathcal{F} = \mathcal{F}_L$ (\mathcal{F}_G). All cases show convergence to the exact form (top black curve) for increasing circuit depth D . The upper bound of D is effectively reduced by increasing η . The black vertical dotted line refers to the exact gap Δ_{exact} . The tilted black open arrow shows how \mathcal{A} evolves as η increases for (a) and (b) $D = 140$ and (e) and (f) 230. The bottom panels indicate (c) and (g) gap-estimate error ε_{gap} and (d) and (h) spectral line-shape error $\varepsilon_{\text{spect}}$ (solid symbols), bounded above by $\varepsilon_{\text{bound}}$ (open symbols), as a function of D for different choices of \mathcal{F} and η . In all simulations, 1024 measurement shots were used, and other parameters are $\theta_j = 0.27\pi$ (uniform over sites), $\delta\omega = \eta/4$, and $L = 2\lceil 7h/\delta\omega \rceil$ [46], where $\lceil x \rceil$ is the ceiling function of x .

$D = 140$ (230) for $p = 1$ (4), allowing a direct comparison between the plots with various η but fixed D .

Either choice of p or \mathcal{F} can change the characteristics of convergence while the overall trends hold. To show this clearly, we measure different types of errors from the data and compare them. First, we define the gap-estimate error:

$$\varepsilon_{\text{gap}} = \frac{|\Delta - \Delta_{\text{exact}}|}{\Delta_{\text{exact}}}, \quad (37)$$

where Δ is a gap estimate obtained using the protocol outlined in Sec. III C and Δ_{exact} is the exact gap as a reference for a small-size system. Figures 4(c) and 4(g) show the evolution of ε_{gap} with D . For each choice of (\mathcal{F}, η) , we can estimate the circuit depth cutoff \tilde{D}_c where ε_{gap} reaches the lower bound. Plateaus arise since the frequency resolution is limited by 2η . We find that \tilde{D}_c decreases for larger η , with an extra shift depending on the choice of \mathcal{F} : $\tilde{D}_{c,G} < \tilde{D}_{c,L}$. Such a distinction occurs because the Gaussian line shape is more concentrated at the center than the Lorentzian case, efficiently suppressing interference with neighbor peaks. Meanwhile, the effect of higher p is not as impressive as we might expect. Comparing the $p = 4$ data with $p = 1$ data, for example, \tilde{D}_c is slightly lower (higher) for $\eta/h = 0.02$ (0.3). In fact, this is nothing but what Fig. 1 implies: For $\eta \rightarrow 0$, $p = 4$ outperforms $p = 1$ in the entire time domain, while that is not the case for large η since $p = 1$ improves more than $p = 4$ at long times.

Another useful measure is the spectral line-shape error (as a square root of the measure known as the coefficient of determination in statistics [48]):

$$\varepsilon_{\text{spect}} = \sqrt{\frac{\sum_{m=0}^{L-1} [\mathcal{A}(\omega_m) - \mathcal{A}_{\text{exact}}(\omega_m)]^2}{\sum_{m=0}^{L-1} [\mathcal{A}(\omega_m) - \mathcal{A}_{\text{av}}]^2}}, \quad (38)$$

where $\mathcal{A}_{\text{av}} = \frac{1}{L} \sum_{m=0}^{L-1} \mathcal{A}(\omega_m)$. Since Eq. (37) measures error only in the main peak center, error may accidentally be reduced when satellite peaks dwell around the main peak for small D . Equation (38), by contrast, accumulates errors in the spectral line shape over the entire frequency domain and therefore provides a more consistent measure. Figures 4(d) and 4(h) show the counterpart to Figs. 4(c) and 4(g) for different choices of (p, \mathcal{F}, η) . The overall trend of $\varepsilon_{\text{spect}}$ matches that of ε_{gap} , but without plateaus since the resolution of $\varepsilon_{\text{spect}}$ is not affected by η .

Last, it is useful to derive the upper bound of Eq. (38). A starting point is the Trotter truncation error $\|\mathcal{F}(t_n)[\rho_M(t_n) - \rho_{\text{exact}}(t_n)]\|$ with the upper bound [Eq. (22)]. Since the spectral norm $\|\cdot\|$ plays a key role in deriving the upper bound, we define $\hat{\mathcal{A}}(\omega_m)$ by replacing $\text{Tr}[\cdot]$ in Eq. (31) with $\|\cdot\|$. Then the upper bound of Eq. (38) has the form

$$\varepsilon_{\text{bound}} = \sqrt{\frac{\sum_{m=0}^{L-1} [\hat{\mathcal{A}}(\omega_m) - \hat{\mathcal{A}}_{\text{exact}}(\omega_m)]^2}{\sum_{m=0}^{L-1} [\hat{\mathcal{A}}(\omega_m) - \hat{\mathcal{A}}_{\text{av}}]^2}}, \quad (39)$$

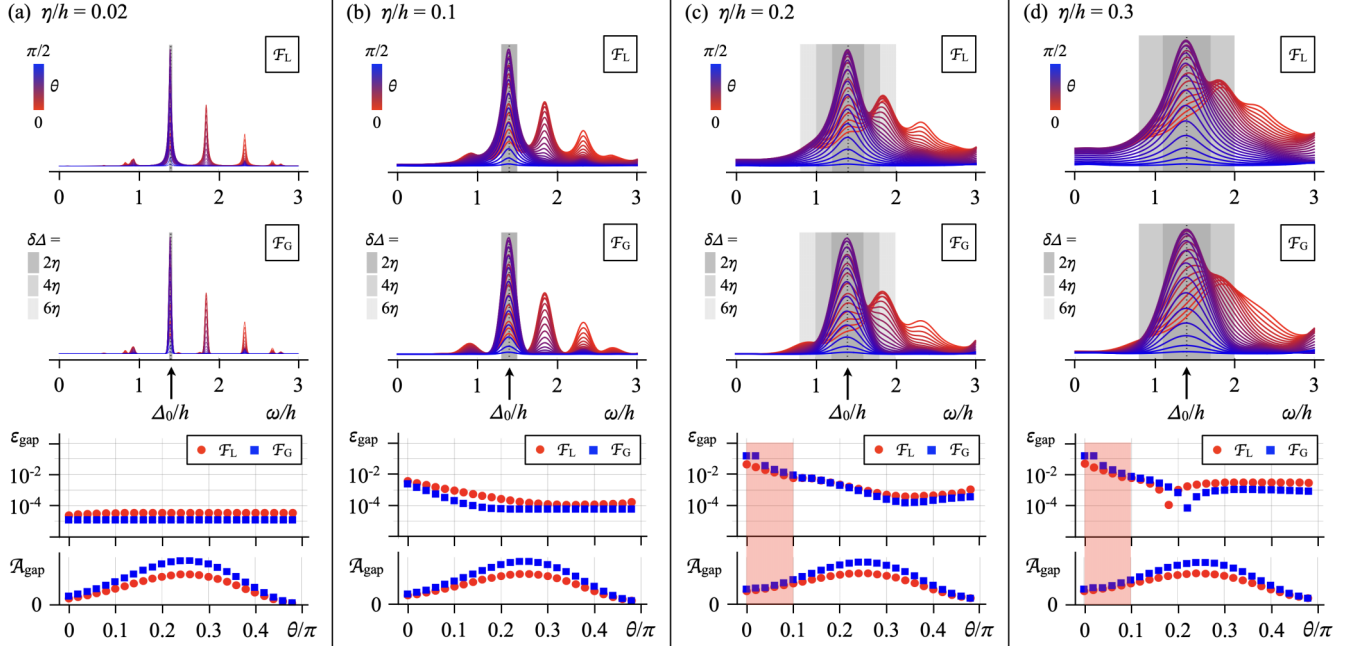


FIG. 5. Simulation results demonstrating the operating range of filtering. The results are compared for different choices of the broadening, (a) $\eta/h = 0.02$, (b) 0.1 , (c) 0.2 , and (d) 0.3 , and the filter $\mathcal{F} \in \{\mathcal{F}_L, \mathcal{F}_G\}$, but with Trotterization set to the order $p = 1$. The top and middle panels show the spectral function \mathcal{A} versus frequency ω for the TFIM with $N = 4$ and $J/h = 0.4$ but different \mathcal{F} . Here, circuit depth D is set to (a) 40 000, (b) 1400, (c) 400, and (d) 140 (satisfying the spectral line-shape error $\varepsilon_{\text{spect}} < 10^{-3}$), and \mathcal{A} 's are sampled with uniformly selected input orientations $\theta_l/\pi = l/50$ and $l \in [0, 24]$ (irrespective of sites). For each θ_l , starting with the initial guess for the energy gap Δ_0 (black vertical dotted line), we search for the peak center close to Δ_0 within the window $[\Delta_0 - \delta\Delta/2, \Delta_0 + \delta\Delta/2]$ by progressively increasing $\delta\Delta$ (gray shading). The bottom panels show the gap-estimate error ε_{gap} and the peak height $\mathcal{A}_{\text{gap}} = \mathcal{A}(\omega = \Delta)$ as a function of θ for both \mathcal{F}_L and \mathcal{F}_G . Red shading indicates the unfavored zone where we set $\varepsilon_{\text{gap}} \gtrsim 10^{-2}$. Other parameters are the same as in Fig. 4.

where $\hat{\mathcal{A}}(\omega_m) = \hat{\mathcal{A}}_{\text{exact}}(\omega_m) + \delta\hat{\mathcal{A}}(\omega_m)$, with

$$\left\{ \begin{array}{l} \hat{\mathcal{A}}_{\text{exact}} \\ \delta\hat{\mathcal{A}} \end{array} \right\} = \frac{\delta t}{2\pi} \text{Re} \sum_{s=\pm} \sum_{n=0}^{L-1} e^{i\omega_m t_{sn}} \mathcal{F}_n \left\{ C^{(p)} t_{sn}^{p+1} / M^p \right\}, \quad (40)$$

and $\hat{\mathcal{A}}_{\text{av}} = \frac{1}{L} \sum_{m=0}^{L-1} \hat{\mathcal{A}}(\omega_m)$. Open symbols in Figs. 4(d) and 4(h) represent Eq. (39), revealing a trend similar to the solid symbols, but with overestimation in the whole range of circuit depth.

B. Operating range of filtering

We just showed that the filtering method can be leveraged to improve the convergence of the hybrid QGE algorithm but only with the input unitary $U_1(\vec{\theta})$ fixed to a certain form. In fact, $U_1(\vec{\theta})$ provides a control knob that allows further investigation of our algorithm. Importantly, the filter has an operating range designed to maximize simulation performance. Specifically, η in the filter is bounded above by spectral resolution set by the algorithm and model. Tuning $\vec{\theta}$ in $U_1(\vec{\theta})$ can impact the resolution by changing relative peak heights. Here, we map out the spectral functions with different ratios of peak heights for different choices of $\vec{\theta}$ to numerically confirm the upper bound of η .

Figure 5 shows simulation results for $N = 4$ and $J/h = 0.4$ for different choices of $\eta/h \in \{0.02, 0.1, 0.2, 0.3\}$. Here, we use $p = 1$ Trotterization. The top and middle panels, assuming $\theta_j = \theta$, i.e., uniform input orientation over sites j , indicate

that tuning $\theta \in [0, \pi/2]$ emphasizes different peaks in \mathcal{A} for the choice of \mathcal{F}_L (top) and \mathcal{F}_G (middle). The gap is estimated starting with an initial guess Δ_0 (indicated by an arrow) and progressively increasing the search window $\delta\Delta$ (gray shading). The bottom panel shows the gap-estimate error ε_{gap} as a function of θ . According to Eq. (35), a gap estimate without filtering is invariant under any choice of θ . This is exemplified by Fig. 5(a), where 2η is far below peak-to-peak resolution and thus ε_{gap} is constant over θ . Meanwhile, filtering broadens each peak by 2η [see Eq. (36)], thus allowing an overlap between neighbor peaks. The tail of neighbor peaks generally forms a slanted background that shifts the peak center of interest here. Figures 5(b)–5(d), in contrast to Fig. 5(a), reveal a nonuniform modification of ε_{gap} over θ , growing for increasing η . Specifically, the modification actively arises in the regime of θ close to zero, where the neighbor peak centered at $\omega/h \approx 1.845$ grows and eventually dominates the main peak. For larger η , a minor peak is buried more easily under the background, thus shifting the peak center from one location to another and lifting ε_{gap} . The choice of \mathcal{F} also affects the above argument since it sets the background in a different form. In Fig. 5(d), for example, \mathcal{F}_G more effectively decreases ε_{gap} than \mathcal{F}_L for $\theta \geq 0.2\pi$, while the reverse is true for $\theta < 0.2\pi$. As mentioned before, this is attributed to the fact that the Gaussian line shape is more concentrated at the center than that in the Lorentzian case. Appendix C describes a toy model to support our argument on peak-center shift. Last, the plots for \mathcal{A}_{gap} , estimated at $\omega = \Delta$, show that one can

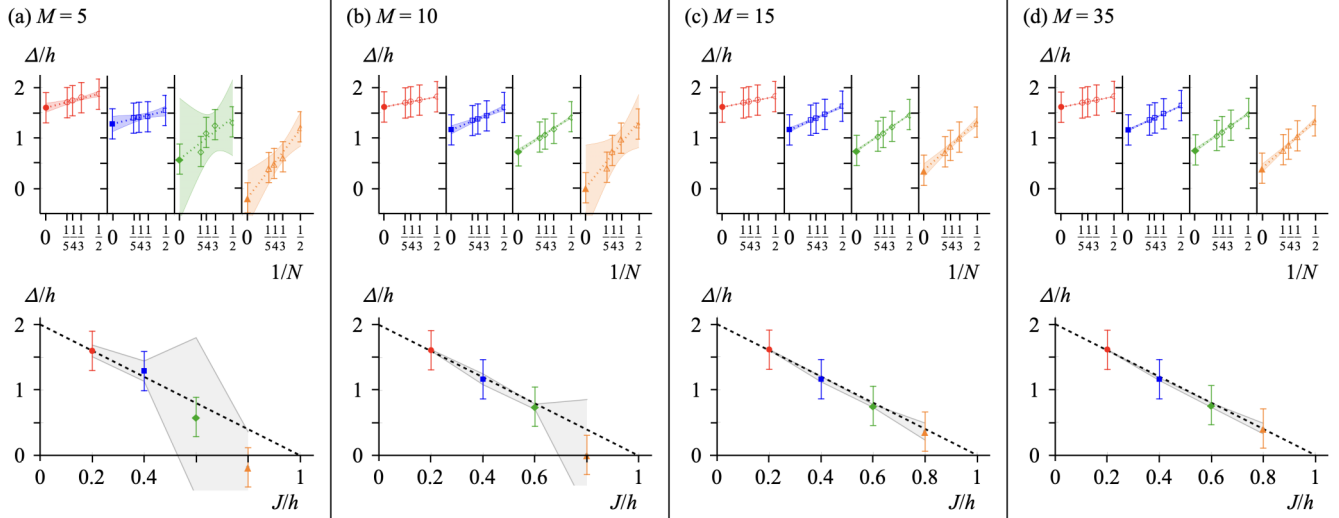


FIG. 6. Stages of construction for the gap-based phase diagram of a quantum paramagnet. In the hybrid QGE simulation, we fix the Trotterization order $p = 1$, the filter $\mathcal{F} = \mathcal{F}_G$, and the broadening $\eta/h = 0.3$. Each column shows progress on convergence for increasing Trotter depth, (a) $M = 5$, (b) 10, (c) 15, and (d) 35. The top panels show finite-size scaling of the energy gap for the TFIM. Open symbols indicate the samples of gap estimates $\{\Delta_{N,J/h}\}$ for $N = 2-5$ and $J/h = 0.2$ (red), 0.4 (blue), 0.6 (green), and 0.8 (orange). Vertical fence symbols set error bounds $[\Delta - \eta, \Delta + \eta]$ around Δ . Solid symbols are an extrapolation to $N \rightarrow \infty$ by linear regression (dotted lines). Colored shading shows the confidence bands with a 95% confidence level. The bottom panels show the gap-based phase diagram of a quantum paramagnet ($J < h$). Solid symbols are the extrapolated data points at $N \rightarrow \infty$ (obtained from the top panels). Gray shading shows the interpolation of the confidence band edges (at $N \rightarrow \infty$) for different J/h . The black dashed line indicates the exact gap $\Delta_{\text{exact}}^{(N \rightarrow \infty)}$. Other parameters are the same as in Fig. 4.

safely avoid the unfavorable zone in θ [red shading in Figs. 5(c) and 5(d)] by maximizing the peak height. As discussed later, this condition can serve as a protocol to construct a phase diagram.

C. Finite-size scaling of a quantum paramagnetic gap

Previously, we demonstrated the performance of the hybrid QGE algorithm using shallow quantum circuits in the filtering method and discussed its validity. Our algorithm can be combined with postprocesses to calculate important physical quantities such as a (gap-based) phase diagram. As a benchmark, we construct the phase diagram of a quantum paramagnet ($J < h$) and compare the simulation result with the exact solution. Here, we focus on the case with $p = 1$, $\mathcal{F} = \mathcal{F}_G$, and $\eta/h = 0.3$.

Construction is organized into three stages. First, from the simulation, we obtain the sample of gap estimates $\{\Delta_{N,J/h}\}$ for $N \in \{2, 3, 4, 5\}$ and $J/h \in \{0.2, 0.4, 0.6, 0.8\}$. For η comparable to the spectral resolution [see Figs. 5(c) and 5(d)], we need a protocol for addressing the range of θ where ε_{gap} stays minimal. As discussed before, a sufficient condition is to maximize the height of a target peak. Open symbols in the top panels of Fig. 6 indicate data sampled in the above manner. Next, for each choice of J/h , we use linear regression to extrapolate the data for $N \in \{2, 3, 4, 5\}$ to $N \rightarrow \infty$ (solid symbols). The result is accompanied by confidence bands (colored shading) that represent misalignment of data points. In the last stage, the extrapolated data are rearranged to construct the phase diagram of a quantum paramagnet. The bottom panels in Fig. 6 show the results. Here, the black dashed lines compare with the exact gap $\Delta_{\text{exact}}^{(N \rightarrow \infty)} = 2|h - J|$ (see Appendix B).

Finally, we confirm convergence of the phase diagram for increasing Trotter depth M . The columns in Fig. 6 are arranged in ascending order of M [in the same way as in Fig. 4(b)]. For small M , Δ is off from Δ_{exact} , and confidence bands are comparable to or exceed error bounds 2η (depending on the choice of J/h), while, for increasing M , they safely move inside 2η and eventually converge to Δ_{exact} .

V. CONCLUSION

We developed a hybrid QGE algorithm using a filtered time series. We found, using the filter, exponential improvement of circuit depth at long times and mapped out the role of various input states to reveal the operating range of filtering. We finally showed how our protocol can be used. We constructed the gap-based paramagnetic phase diagram for a minimal spin model, which demonstrates how a quantum device can offer memory advantage in finite-size extrapolation of energy gaps.

Further improvements by, e.g., Cartan decomposition [49] and Bayesian methods [16,17,50] could allow applications to many-body models requiring more gates to implement time evolution. Our approach can also be applied to hybrid DMFT algorithms [32–34], in which speedup and noise resilience were recently observed [34], and a recent proposal for a measurement-based hybrid algorithm for eigenvalue estimation [51].

ACKNOWLEDGMENTS

We acknowledge support from AFOSR (Grants No. FA2386-21-1-4081, No. FA9550-19-1-0272, and No. FA9550-23-1-0034) and ARO (Grants No. W911NF2210247

and No. W911NF2010013). We thank A. F. Kemper and P. Roushan for insightful discussions. We acknowledge the use of IBM Quantum services for this work.

The views expressed are those of the authors and do not reflect the official policy or position of IBM or the IBM Quantum team.

APPENDIX A: EXPLICIT FORMS OF EQS. (23)–(25) FOR THE TFIM

Here, using Eq. (27) for the TFIM, we explicitly calculate the spectral norms in Eqs. (23)–(25). The commutators of H_1 and H_2 of interest can be successively derived as follows:

$$[H_1, H_2] = 2iJh \sum_{j=0}^{N-2} (\sigma_j^y \sigma_{j+1}^z + \sigma_j^z \sigma_{j+1}^y), \quad (\text{A1})$$

$$[H_1, [H_1, H_2]] = -8J^2h \left[\sum_{j=0}^{N-1} \sigma_j^x + \sum_{j=0}^{N-3} \sigma_j^z \sigma_{j+1}^x \sigma_{j+2}^z \right], \quad (\text{A2})$$

$$[H_2, [H_1, H_2]] = -8Jh^2 \sum_{j=0}^{N-2} (\sigma_j^y \sigma_{j+1}^y - \sigma_j^z \sigma_{j+1}^z), \quad (\text{A3})$$

$$\begin{aligned} [H_1, [H_1, [H_2, [H_1, H_2]]]] &= [H_1, [H_2, [H_1, [H_1, H_2]]]] \\ &= -64J^3h^2 \left[\sum_{j=0}^{N-2} \sigma_j^y \sigma_{j+1}^y - \sum_{j=0}^{N-4} \sigma_j^z \sigma_{j+1}^x \sigma_{j+2}^z \sigma_{j+3}^z \right], \quad (\text{A4}) \end{aligned}$$

$$\begin{aligned} [H_2, [H_1, [H_2, [H_1, H_2]]]] &= [H_2, [H_2, [H_1, [H_1, H_2]]]] \\ &= 64J^2h^3 \sum_{j=0}^{N-3} (\sigma_j^y \sigma_{j+1}^x \sigma_{j+2}^y - \sigma_j^z \sigma_{j+1}^x \sigma_{j+2}^z). \quad (\text{A5}) \end{aligned}$$

All others are connected with Eqs. (A2) and (A3):

$$[H_\gamma, [H_1, [H_1, [H_1, H_2]]]] = 8J^2[H_\gamma, [H_1, H_2]], \quad (\text{A6})$$

$$[H_\gamma, [H_2, [H_2, [H_1, H_2]]]] = 16h^2[H_\gamma, [H_1, H_2]], \quad (\text{A7})$$

where $\gamma \in \{1, 2\}$. In the above derivation, we used the identities $[AB, C] = A[B, C] + [A, C]B$ for matrices A, B , and C , $[\sigma^\alpha, \sigma^\beta] = 2i\varepsilon_{\alpha\beta\gamma}\sigma^\gamma$, and $\{\sigma^\alpha, \sigma^\beta\} = 2\delta_{\alpha\beta}I$, with $\delta_{\alpha\beta}$ being the Kronecker delta, $\varepsilon_{\alpha\beta\gamma}$ being the Levi-Civita symbol, and $\alpha, \beta, \gamma \in \{x, y, z\}$. For the spectral norms of Eqs. (A1)–(A7), we apply the properties $\|cA\| = |c|\|A\|$, $\|AB\| \leq \|A\|\|B\|$, $\|A+B\| \leq \|A\| + \|B\|$, and $\|e^{iA}\| = 1$ if $A = A^\dagger$, where A and B are matrices and c is a scalar. It turns out that the upper bounds of the commutators are summarized as

$$\|[\tilde{H}_1, \tilde{H}_2]\| \leq 4(N-1), \quad (\text{A8})$$

$$\|[\tilde{H}_\gamma, [\tilde{H}_1, \tilde{H}_2]]\| \leq 16(N-1), \quad (\text{A9})$$

$$\|[\tilde{H}_\gamma, [\tilde{H}_\lambda, [\tilde{H}_\lambda, [\tilde{H}_1, \tilde{H}_2]]]]\| \leq 128(N-2), \quad (\text{A10})$$

$$\|[\tilde{H}_\gamma, [\tilde{H}_\lambda, [\tilde{H}_\lambda, [\tilde{H}_1, \tilde{H}_2]]]]\| \leq 128\lambda(N-1), \quad (\text{A11})$$

where $\tilde{H}_1 = H_1/|J|$, $\tilde{H}_2 = H_2/|h|$, $\gamma, \lambda \in \{1, 2\}$, and $\bar{\lambda} = 1(2)$ if $\lambda = 2(1)$. Equations (A8)–(A11) allow the derivation of the upper bounds of Eqs. (23)–(25) and therefore Eq. (22).

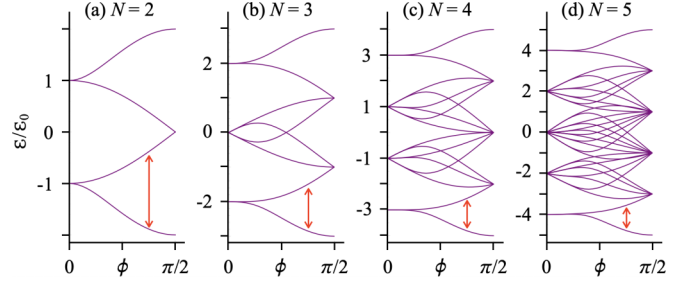


FIG. 7. Energy spectrum of the TFIM for $N = 2-5$ as a function of $\phi [= \cot^{-1}(J/h)]$. Here, we have a ferromagnet (paramagnet) at $\phi = 0$ ($\pi/2$), and the red arrow indicates the lowest energy gap of the quantum paramagnet ($\pi/4 < \phi \leq \pi/2$).

APPENDIX B: REFERENCE FORMULAS FOR THE ENERGY GAP OF THE TFIM

Here, we derive the reference formulas for the energy gap of the TFIM using (1) perturbation theory and (2) exact methods.

1. Initial guess of the energy gap

Figure 7 shows the energy spectrum of the TFIM for $N = 2-5$, where the lowest energy gap of interest is indicated by the red arrow. In the hybrid QGE algorithm, gap estimation generally requires an initial guess for the energy gap. For this purpose, we consider a generally applicable procedure: perturbation expansion [41]. In our case, we perturb in powers of J/h to find the approximate energy gap of the quantum paramagnet. For the TFIM with N spins, a spin flip from the paramagnetic ground state $\prod_{j=1}^N |0\rangle_j$ requires excitation energy $2h - 2J$ for $N - 2$ bulk spins and $2h - J$ for two boundary spins. Averaging excitation energies over all spins yields an approximate formula for the energy gap:

$$\begin{aligned} \Delta_0/h &= [(N-2)(2h-2J) + 2(2h-J)]/(Nh) \\ &= 2[1 - (1-1/N)J/h], \quad (\text{B1}) \end{aligned}$$

which is reduced to the case with periodic boundaries [41],

$$\Delta_0/h|_{N \rightarrow \infty} = 2(1 - J/h). \quad (\text{B2})$$

This expression for Δ_0 shows how we derived the initial guess for the gap and also establishes that perturbative methods can, in other models, be used to define the guess.

2. Exact energy gap

The TFIM is tractable in the limit $N \rightarrow \infty$. An exact solution provides a reference to compare with the simulation result. Using the Jordan-Wigner transformation [52], $\sigma_j^x = 1 - 2c_j^\dagger c_j$ and $\sigma_j^z = -\prod_{k<j} (1 - 2c_k^\dagger c_k)(c_j + c_j^\dagger)$, the TFIM is mapped to the Kitaev model describing a p -wave superconductor:

$$H_K = -w \sum_{j=1}^{N-1} (c_j^\dagger c_{j+1} + c_j^\dagger c_{j+1}^\dagger + \text{H.c.}) - \mu \sum_{j=1}^N \delta n_j, \quad (\text{B3})$$

where $w(=J)$ is the hopping or pairing energy, $\mu(=-2h)$ is the chemical potential, and $\delta n_j = c_j^\dagger c_j - 1/2$. Assuming

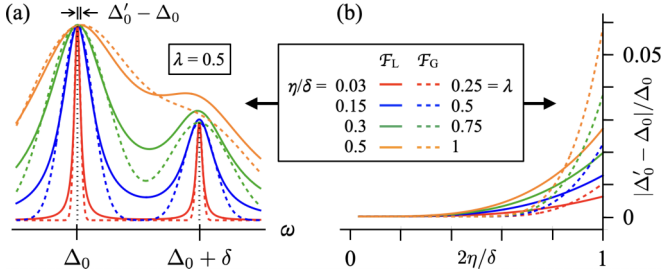


FIG. 8. (a) Spectral function for two peaks separated by $\delta/\Delta_0 = 0.6$ with different choices of the broadening η but fixed relative height $\lambda = 0.5$. Here, all plots are normalized, and the vertical black dotted lines indicate the reference to the peak centers at $\omega = \Delta_0, \Delta_0 + \delta$ for $\eta \rightarrow 0$. (b) Peak-center shift $|\Delta'_0 - \Delta_0|/\Delta_0$ as a function of η for different choices of λ and the filter $\mathcal{F} \in \{\mathcal{F}_L, \mathcal{F}_G\}$.

periodic boundaries, H_K can be diagonalized by the Bogoliubov transformation [41]. The result yields the exact form of the upper and lower energy bands:

$$\mathcal{E}_{\mathbf{k}}^{\pm} = \pm \sqrt{J^2 + h^2 - 2Jh \cos(ka)}, \quad (\text{B4})$$

where k is momentum and a is the lattice constant. The lowest energy gap between two bands is therefore given by the energy difference at $\mathbf{k} = 0$:

$$\Delta_{\text{exact}}^{(N \rightarrow \infty)} = \mathcal{E}_{\mathbf{k}=0}^+ - \mathcal{E}_{\mathbf{k}=0}^- = 2|h - J|, \quad (\text{B5})$$

consistent with Eq. (B2) in the paramagnetic regime ($J < h$).

APPENDIX C: TOY MODEL FOR PEAK-CENTER SHIFT

Here, we describe a toy model for peak-center shift to support the argument in Sec. IV B. In general, peak centers are subject to shifting when the separation between peaks is comparable to the broadening of each peak. To show this, we model the spectral function for two peaks separated by δ :

$$\mathcal{A}(\omega) \propto \mathcal{A}_0(\omega - \Delta_0) + \lambda \mathcal{A}_0(\omega - \Delta_0 - \delta), \quad (\text{C1})$$

where we set

$$\mathcal{A}_0(\omega) = \begin{cases} \frac{1}{\pi} \frac{\eta}{\omega^2 + \eta^2}, & \text{Lorentzian,} \\ \frac{1}{\sqrt{2\pi}\sigma} e^{-\frac{\omega^2}{2\sigma^2}}, & \text{Gaussian,} \end{cases} \quad (\text{C2})$$

describing an isolated Lorentzian (Gaussian) peak associated with the filter $\mathcal{F}_{L(G)}$; $\eta = \sigma \sqrt{2 \ln 2}$; and λ controls the second peak height. Figure 8(a) shows how much the original line shape is modified when two peaks overlap in the tail for different choices of η but fixed λ . In Fig. 8(b), we focus on the first peak at $\omega = \Delta_0$ and measure the peak-center shift $|\Delta'_0 - \Delta_0|/\Delta_0$ as a function of η for different choices of λ . The result implies that (1) the peak-center shift is enhanced for increasing η , (2) it is enhanced (suppressed) for increasing (decreasing) symmetry between peaks, and (3) $\mathcal{F}_{L(G)}$ induces a larger shift than $\mathcal{F}_{G(L)}$ for $2\eta/\delta \lesssim (\gtrsim) 0.85$.

- [1] R. P. Feynman, Simulating physics with computers, *Int. J. Theor. Phys.* **21**, 467 (1982).
- [2] S. Lloyd, Universal quantum simulators, *Science* **273**, 1073 (1996).
- [3] D. S. Abrams and S. Lloyd, Quantum algorithm providing exponential speed increase for finding eigenvalues and eigenvectors, *Phys. Rev. Lett.* **83**, 5162 (1999).
- [4] M. A. Nielsen and I. L. Chuang, *Quantum Computation and Quantum Information* (Cambridge University Press, Cambridge, 2010).
- [5] M.-H. Yung, J. D. Whitfield, S. Boixo, D. G. Tempel, and A. Aspuru-Guzik, Introduction to quantum algorithms for physics and chemistry, in *Quantum Information and Computation for Chemistry* (Wiley, Hoboken, NJ, 2014), Chap. 3, pp. 67–106.
- [6] A. Kitaev, Quantum measurements and the Abelian stabilizer problem, *Electr. Coll. Comput. Complex.* TR96-003 (1996).
- [7] R. Somma, G. Ortiz, J. E. Gubernatis, E. Knill, and R. Laflamme, Simulating physical phenomena by quantum networks, *Phys. Rev. A* **65**, 042323 (2002).
- [8] R. D. Somma, Quantum eigenvalue estimation via time series analysis, *New J. Phys.* **21**, 123025 (2019).
- [9] T. E. O'Brien, B. Tarasinski, and B. M. Terhal, Quantum phase estimation of multiple eigenvalues for small-scale (noisy) experiments, *New J. Phys.* **21**, 023022 (2019).
- [10] T. E. O'Brien, S. Polla, N. C. Rubin, W. J. Huggins, S. McArdle, S. Boixo, J. R. McClean, and R. Babbush, Error mitigation via verified phase estimation, *PRX Quant.* **2**, 020317 (2021).
- [11] L. Lin and Y. Tong, Heisenberg-limited ground-state energy estimation for early fault-tolerant quantum computers, *PRX Quant.* **3**, 010318 (2022).
- [12] G. Wang, D. S. França, R. Zhang, S. Zhu, and P. D. Johnson, Quantum algorithm for ground state energy estimation using circuit depth with exponentially improved dependence on precision, *Quantum* **7**, 1167 (2023).
- [13] Z. Ding and L. Lin, Even shorter quantum circuit for phase estimation on early fault-tolerant quantum computers with applications to ground-state energy estimation, *PRX Quant.* **4**, 020331 (2023).
- [14] Z. Ding and L. Lin, Simultaneous estimation of multiple eigenvalues with short-depth quantum circuit on early fault-tolerant quantum computers, *Quantum* **7**, 1136 (2023).
- [15] D. Wecker, M. B. Hastings, N. Wiebe, B. K. Clark, C. Nayak, and M. Troyer, Solving strongly correlated electron models on a quantum computer, *Phys. Rev. A* **92**, 062318 (2015).
- [16] I. Zintchenko and N. Wiebe, Randomized gap and amplitude estimation, *Phys. Rev. A* **93**, 062306 (2016).
- [17] K. Sugisaki, C. Sakai, K. Toyota, K. Sato, D. Shiomi, and T. Takui, Bayesian phase difference estimation: A general quantum algorithm for the direct calculation of energy gaps, *Phys. Chem. Chem. Phys.* **23**, 20152 (2021).
- [18] A. E. Russo, K. M. Rudinger, B. C. A. Morrison, and A. D. Baczewski, Evaluating energy differences on a quantum computer with robust phase estimation, *Phys. Rev. Lett.* **126**, 210501 (2021).

- [19] Y. Matsuzaki, H. Hakoshima, K. Sugisaki, Y. Seki, and S. Kawabata, Direct estimation of the energy gap between the ground state and excited state with quantum annealing, *Jpn. J. Appl. Phys.* **60**, SBBI02 (2021).
- [20] H. F. Trotter, On the product of semi-groups of operators, *Proc. Am. Math. Soc.* **10**, 545 (1959).
- [21] M. Suzuki, Generalized Trotter's formula and systematic approximations of exponential operators and inner derivations with applications to many-body problems, *Commun. Math. Phys.* **51**, 183 (1976).
- [22] T. Barthel and Y. Zhang, Optimized Lie–Trotter–Suzuki decompositions for two and three non-commuting terms, *Ann. Phys. (NY)* **418**, 168165 (2020).
- [23] A. M. Childs, Y. Su, M. C. Tran, N. Wiebe, and S. Zhu, Theory of Trotter error with commutator scaling, *Phys. Rev. X* **11**, 011020 (2021).
- [24] A. Peruzzo, J. McClean, P. Shadbolt, M.-H. Yung, X.-Q. Zhou, P. J. Love, A. Aspuru-Guzik, and J. L. O'Brien, A variational eigenvalue solver on a photonic quantum processor, *Nat. Commun.* **5**, 4213 (2014).
- [25] J. R. McClean, R. Babbush, P. J. Love, and A. Aspuru-Guzik, Exploiting locality in quantum computation for quantum chemistry, *J. Phys. Chem. Lett.* **5**, 4368 (2014).
- [26] D. Wecker, M. B. Hastings, and M. Troyer, Progress towards practical quantum variational algorithms, *Phys. Rev. A* **92**, 042303 (2015).
- [27] J. R. McClean, J. Romero, R. Babbush, and A. Aspuru-Guzik, The theory of variational hybrid quantum-classical algorithms, *New J. Phys.* **18**, 023023 (2016).
- [28] J. Tilly, H. Chen, S. Cao, D. Picozzi, K. Setia, Y. Li, E. Grant, L. Wossnig, I. Rungger, G. H. Booth, and J. Tennyson, The variational quantum eigensolver: A review of methods and best practices, *Phys. Rep.* **986**, 1 (2022).
- [29] J. R. McClean, S. Boixo, V. N. Smelyanskiy, R. Babbush, and H. Neven, Barren plateaus in quantum neural network training landscapes, *Nat. Commun.* **9**, 4812 (2018).
- [30] J. Lee, D. W. Berry, C. Gidney, W. J. Huggins, J. R. McClean, N. Wiebe, and R. Babbush, Even more efficient quantum computations of chemistry through tensor hypercontraction, *PRX Quant.* **2**, 030305 (2021).
- [31] B. M. Terhal, Quantum error correction for quantum memories, *Rev. Mod. Phys.* **87**, 307 (2015).
- [32] B. Bauer, D. Wecker, A. J. Millis, M. B. Hastings, and M. Troyer, Hybrid quantum-classical approach to correlated materials, *Phys. Rev. X* **6**, 031045 (2016).
- [33] T. Keen, T. Maier, S. Johnston, and P. Lougovski, Quantum-classical simulation of two-site dynamical mean-field theory on noisy quantum hardware, *Quantum Sci. Technol.* **5**, 035001 (2020).
- [34] T. Steckmann, T. Keen, E. Kökcü, A. F. Kemper, E. F. Dumitrescu, and Y. Wang, Mapping the metal-insulator phase diagram by algebraically fast-forwarding dynamics on a cloud quantum computer, *Phys. Rev. Res.* **5**, 023198 (2023).
- [35] W.-R. Lee, N. M. Myers, and V. W. Scarola, Self-embedded fault tolerance in quantum gap estimation with trial-state optimization (unpublished).
- [36] A. M. Childs, D. Maslov, Y. Nam, N. J. Ross, and Y. Su, Toward the first quantum simulation with quantum speedup, *Proc. Natl. Acad. Sci. USA* **115**, 9456 (2018).
- [37] A. M. Childs and Y. Su, Nearly optimal lattice simulation by product formulas, *Phys. Rev. Lett.* **123**, 050503 (2019).
- [38] M. C. Tran, S. K. Chu, Y. Su, A. M. Childs, and A. V. Gorshkov, Destructive error interference in product-formula lattice simulation, *Phys. Rev. Lett.* **124**, 220502 (2020).
- [39] H. Haug and A. Jauho, *Quantum Kinetics in Transport and Optics of Semiconductors*, Springer Series in Solid-State Sciences (Springer, Berlin, 2007).
- [40] The self-energy may be set up to describe spin-dependent scattering processes. Here, we avoid those cases since they generally need additional Trotterization for circuit implementation.
- [41] S. Sachdev, *Quantum Phase Transitions* (Cambridge University Press, Cambridge, 2011).
- [42] K. Vogel and H. Risken, Determination of quasiprobability distributions in terms of probability distributions for the rotated quadrature phase, *Phys. Rev. A* **40**, 2847 (1989).
- [43] P. Duhamel and M. Vetterli, Fast fourier transforms: A tutorial review and a state of the art, *Signal Process.* **19**, 259 (1990).
- [44] In contrast to QGE, the time propagator for eigenvalue estimation is not represented in a density-matrix form. For eigenvalue estimation, instead, a Hadamard test circuit is constructed to return the real and imaginary parts of the time propagator when a single ancilla qubit is measured (see Refs. [7,11], for example).
- [45] QISKIT code for the hybrid QGE algorithm, https://github.com/wrlee7609/hybrid_quantum_gap_estimation.
- [46] For the filter \mathcal{F} with the broadening η , it is enough to choose the frequency unit $\delta\omega = \eta/4$, implying that only four sampling points are contained within the half width of a peak. The sampling size is set to $L = 2\lceil 7h/\delta\omega \rceil$, yielding a frequency window larger than the bandwidth of the many-body model we consider. To get better precision in gap estimation, the sampling data can be interpolated whatever we take for (\mathcal{F}, η) .
- [47] M. Heyl, P. Hauke, and P. Zoller, Quantum localization bounds Trotter errors in digital quantum simulation, *Sci. Adv.* **5**, eaau8342 (2019).
- [48] D. Chicco, M. J. Warrens, and G. Jurman, The coefficient of determination R-squared is more informative than SMAPE, MAE, MAPE, MSE and RMSE in regression analysis evaluation, *PeerJ Comput. Sci.* **7**, e623 (2021).
- [49] E. Kökcü, T. Steckmann, Y. Wang, J. K. Freericks, E. F. Dumitrescu, and A. F. Kemper, Fixed depth Hamiltonian simulation via Cartan decomposition, *Phys. Rev. Lett.* **129**, 070501 (2022).
- [50] N. Wiebe and C. Granade, Efficient Bayesian phase estimation, *Phys. Rev. Lett.* **117**, 010503 (2016).
- [51] W.-R. Lee, Z. Qin, R. Raussendorf, E. Sela, and V. W. Scarola, Measurement-based time evolution for quantum simulation of fermionic systems, *Phys. Rev. Res.* **4**, L032013 (2022).
- [52] P. Jordan and E. Wigner, Über das Paulische Äquivalenzverbot, *Z. Phys.* **47**, 631 (1928).